Mon. Not. R. Astron. Soc. **000**, 1–?? (2009) Printed 3 November 2014 (MN LATEX style file v2.2)

How realistic UV spectra and X-rays suppress the abundance of direct collapse black holes

M. A. Latif, ⋆[1] S. Bovino,[1] T. Grassi, [2,3] D. R. G. Schleicher, [1] M. Spaans[4]
[1] *Institut für Astrophysik, Georg-August-Universität, Friedrich-Hund-Platz 1, D-37077 Göttingen, Germany*
[2] *Centre for Star and Planet Formation, Natural History Museum of Denmark, Øster Voldgade 5-7, DK-1350 Copenhagen, Denmark*
[3] *Niels Bohr Institute, University of Copenhagen, Juliane Maries Vej 30, DK-2100 Copenhagen, Denmark*
[4] *Kapteyn Astronomical Institute, University of Groningen, P.O. Box 800, 9700 AV Groningen, The Netherlands*

arXiv:1408.3061v2 [astro-ph.GA] 31 Oct 2014

ABSTRACT

Observations of high redshift quasars at $z > 6$ indicate that they harbor supermassive black holes (SMBHs) of a billion solar masses. The direct collapse scenario has emerged as the most plausible way to assemble SMBHs. The nurseries for the direct collapse black holes are massive primordial halos illuminated with an intense UV flux emitted by population II (Pop II) stars. In this study, we compute the critical value of such a flux ($J_{21}^{\rm crit}$) for realistic spectra of Pop II stars through three-dimensional cosmological simulations. We derive the dependence of $J_{21}^{\rm crit}$ on the radiation spectra, on variations from halo to halo, and on the impact of X-ray ionization. Our findings show that the value of $J_{21}^{\rm crit}$ is a few times 10^4 and only weakly depends on the adopted radiation spectra in the range between $T_{\rm rad} = 2 \times 10^4 - 10^5$ K. For three simulated halos of a few times 10^7 $M_\odot$, $J_{21}^{\rm crit}$ varies from $2 \times 10^4 - 5 \times 10^4$. The impact of X-ray ionization is almost negligible and within the expected scatter of $J_{21}^{\rm crit}$ for background fluxes of $J_{\rm X,21} \leq 0.1$. The computed estimates of $J_{21}^{\rm crit}$ have profound implications for the quasar abundance at $z = 10$ as it lowers the number density of black holes forming through an isothermal direct collapse by a few orders of magnitude below the observed black holes density. However, the sites with moderate amounts of H_2 cooling may still form massive objects sufficient to be compatible with observations.

Key words: methods: numerical – cosmology: theory – early Universe – galaxies: formation

1 INTRODUCTION

Observations of quasars at $z > 6$ unfold the presence of supermassive black holes (SMBHs) of 10^9 $M_\odot$ (Fan et al. 2003, 2006; Willott et al. 2010; Mortlock et al. 2011; Venemans et al. 2013). The formation of such massive objects within the first billion years after the Big Bang is an open question. Various scenarios for the assembling of SMBHs have been proposed which include the remnants of the first stars, stellar dynamical process in a dense nuclear cluster and the collapse of a protogalactic gas cloud into a so-called direct collapse black hole (DCBH). The most natural candidates to assemble SMBHs are the stellar mass black holes formed through the collapse of the first generation of stars.

According to the hierarchical scenario of structure formation population III (Pop III) stars are formed in minihalos of $10^5 - 10^6$ $M_\odot$ at $z \sim 20 - 30$. The three dimensional cosmological simulations exploring the formation of Pop III stars including their radiation feedback show that they can reach maximum masses of a few hundred solar (Hirano et al. 2014; Susa et al. 2014). The feedback from stellar mass black holes limits the accretion and makes them difficult to grow in the available time (Johnson & Bromm 2007; Alvarez et al. 2009). However, cyclic episodes of super Eddington accretion (Madau et al. 2014) or merging of many stellar mass black holes (Haiman 2004; Tanaka & Haiman 2009) may help them to grow faster. Another way could be the formation of a dense nuclear cluster in metal enriched halo which collapses via the stellar dynamical processes (Devecchi & Volonteri 2009; Lupi et al. 2014) and provides a black hole seed of a few thousand solar masses. An alternative route could be the formation of heavy seeds of $10^4 - 10^6$ $M_\odot$ through rapid inflow of gas provided that fragmentation remains inhibited (Bromm & Loeb 2003; Spaans & Silk 2006; Begelman et al. 2006; Lodato & Natarajan 2006; Latif et al. 2014). Further details about these mechanisms can be found in reviews (Volonteri 2010; Haiman 2012).

⋆ Corresponding author: mlatif@astro.physik.uni-goettingen.de

© 2009 RAS

The direct collapse scenario has gained a lot of interest during the past decade as it provides massive seeds which can later grow at relatively moderate accretion rates to form SMBHs. Numerical simulations show that massive primordial halos of $10^7 - 10^8$ $M_\odot$ forming at $z \sim 15 - 20$ collapse monolithically in the absence of H_2 cooling (Wise et al. 2008; Regan & Haehnelt 2009; Latif et al. 2011) and are the potential birthplaces of DCBHs. These studies employed a Jeans resolution of 16 cells insufficient to resolve turbulent eddies. Our recent studies show that resolving turbulence mandates a Jeans resolution of ≥ 32 cells (Latif et al. 2013b,c) which also helps in regulating the angular momentum. Latif et al. (2013a) show that fragmentation occurs occasionally but does not prevent the formation of massive objects and large accretion rates of 1 $M_\odot/yr$ are observed. The presence of strong magnetic fields amplified via the small scale dynamo further aids in suppressing fragmentation (Latif et al. 2013d, 2014).

The most recent high resolution studies following the evolution after the initial collapse demonstrate that massive seeds of 10^5 $M_\odot$ are formed (Latif et al. 2013e; Regan et al. 2014). Theoretical studies suggest that such supermassive stars are the potential embryos of DCBHs (Begelman 2010; Ball et al. 2012; Hosokawa et al. 2013). The work by Schleicher et al. (2013) suggests that for accretion rates < 0.1 $M_\odot/yr$ supermassive stars (stars of $10^3 - 10^6$ $M_\odot$) are expected to form while for > 0.1 $M_\odot/yr$ quasi-stars (stars with BHs in their interior) are the expected outcome. Ferrara et al. (2014) have computed the initial mass function of DCBHs from merger tree simulations and found that their mass distribution depends whether their progenitors were polluted or remained pristine.

It is imperative for the feasibility of this scenario that gas in the halo must be of primordial composition and the formation of molecular hydrogen remains inhibited. The latter mandates the presence of an intense UV flux below the Lyman limit (13.6 eV) to suppress the H_2 formation (Schleicher et al. 2010; Latif et al. 2011). Th strength of such a UV flux is much higher than expected background UV field (Dijkstra et al. 2014) and can be achieved in the vicinity of a star forming galaxy (Dijkstra et al. 2008; Agarwal et al. 2012) or even in a synchronized pair of halos (Visbal et al. 2014).

The main pathway for the formation of H_2 in primordial gas is:

$$H + e^- \rightarrow H^- + \gamma \quad (1)$$

$$H + H^- \rightarrow H_2 + e^-. \quad (2)$$

The formation of H_2 can be quenched either by destroying H_2 or H^-. Photons with energy between 11.2-13.6 eV are absorbed in the Lyman-Werner bands of H_2 and dissociate it shortly after putting it into an excited state, this is known as the Solomon process. On the other hand, H^- is photo-detached by photons above 0.76 eV. The reactions for these processes are the following:

$$H_2 + \gamma_{LW} \rightarrow H + H \quad (3)$$

$$H^- + \gamma_{0.76} \rightarrow H + e^- \quad (4)$$

The former process (i.e. equation 3) is efficient for stars with $T_{\rm rad} = 10^5$ K while the stars with $T_{\rm rad} = 10^4$ K are efficient in photo-detachment of H^-.

The critical strength of the radiation flux (hereafter, $J_{21}^{\rm crit}$) above which the formation of H_2 remains suppressed has been computed both from one-zone and three dimensional simulations (Omukai 2001; Shang et al. 2010; Latif et al. 2014). The value of $J_{21}^{\rm crit}$ depends on the spectral shape of radiation field. It is commonly presumed that such UV flux is emitted by the first or second generation of stars using idealized spectra with black body radiation temperatures of 10^5 or 10^4 K. The value of $J_{21}^{\rm crit}$ for population II (Pop II) stars assuming idealized spectra of 10^4 K was found to be about two orders of magnitude lower than Pop III stars. Agarwal et al. (2012) performed N-body simulations along with semi-analytical models and found that Pop III are unable to produce the required critical flux for the DCBHs sites (see their Fig. 6) as they have very short lives and are less abundant. At the same time, trace amount of dust or metals are sufficient to produce Pop II stars (Omukai et al. 2005; Cazaux & Spaans 2009; Dopcke et al. 2013; Safranek-Shrader et al. 2014; Bovino et al. 2014) which can more easily provide the flux to produce the observed abundance of quasars. As we show in this study using realistic Pop II spectra the critical value of the flux becomes comparable to that of Pop III stars and does not depend much on the stellar population.

For realistic spectra of Pop II stars, $T_{\rm rad}$ is expected to be between $10^4 - 10^5$ K (Leitherer et al. 1999; Schaerer 2003). In a recent study, Sugimura et al. (2014) have computed Pop II spectra from the stellar synthesis code STARBURST (Leitherer et al. 1999) and shown that the effect of realistic spectra can be mimicked by black body spectra with radiation temperatures between $10^4 - 10^5$ K. Their Fig. 6 demonstrates that the value of $J_{21}^{\rm crit}$ solely depends on the ratio of the H^- to H_2 photo-dissociation rates and that black body radiation spectra with temperatures between $10^4 - 10^5$ K can reproduce the results of realistic Pop II spectra. The value of $J_{21}^{\rm crit}$ from their one-zone model varies from 1000-1400. They further found that $J_{21}^{\rm crit}$ does not depend on the age or metallicity for constant star formation and even decreases for instantaneous star formation in young metal poor galaxies, contrary to the findings of Agarwal & Khochfar (2014).

Such actively star forming galaxies also produce X-rays as they host massive stars, X-ray binaries and possibly mini-quasars (Kuhlen & Madau 2005; Jeon et al. 2014; Schober et al. 2014; Hummel et al. 2014). X-rays have a long mean free path (small absorption cross-section for HI) and can easily escape to build up a cosmic X-ray background. They can photo-ionize/photo-heat the gas and may boost the formation of molecular hydrogen by enhancing the degree of ionization (Haiman et al. 1997; Glover & Brand 2003). Inayoshi & Omukai (2011a) performed one-zone calculations to study the impact of the X-ray background flux in the context of the direct collapse scenario and found that it raises the critical threshold for UV by a factor 5 ($J_{21}^{\rm crit} \propto J_{\rm X}^{1/2}$) by boosting H_2 formation.

In this study, we compute the value of $J_{21}^{\rm crit}$ for realistic Pop II spectra. To achieve this goal, we perform three-dimensional cosmological simulations for three distinct massive primordial halos of $10^7 - 10^8$ $M_\odot$ at $z > 10$ by employing a comprehensive chemical model. We further compute the dependence of $J_{21}^{\rm crit}$ on the radiation spectra for $T_{\rm rad}$ between $10^4 - 10^5$ K, on variations from halo to halo, and on the

impact of cosmic X-ray ionization. This is the first study exploring the impact of both UV and X-ray background radiation via three-dimensional cosmological simulations with a fixed Jeans resolution of 32 cells and employing a higher order chemical solver (see Bovino et al. 2013). We implement a comprehensive chemical model which takes into account all the chemical and thermal process relevant for this study. This work has significant implications for the expected number density of DCBHs as it provides constraints necessary for their formation.

The article is organized in the following way. In section 2, we provide the details of numerical methods and chemical model employed in this work. We present our findings in section 3 and confer our conclusions in section 4.

2 COMPUTATIONAL METHODS

The simulations presented in this work are performed with the open source code ENZO[1] (Bryan et al. 2014) which is an adaptive mesh refinement, grid based, parallel cosmological simulations code. The piece-wise parabolic solver is used to solve the hydrodynamics equations which is an improved form of the Godunov method (Colella & Woodward 1984). It makes use of the particle mesh technique to solve the dark matter (DM) dynamics and the multi-grid Poisson solver to compute the gravity.

Our simulations are commenced with cosmological initial conditions selected from Gaussian random fields at $z = 100$. We first perform simulation with a uniform grid resolution of 128^3 cells for hydrodynamics and 128^3 dark matter particles to select the most massive halos at redshift 15 using the friend of friends algorithm (Turk et al. 2011). Our computational volume has a comoving size of 1 Mpc/h. The parameters from the WMAP seven years data (Jarosik et al. 2011) are used for generating the initial conditions. We rerun the simulations by employing two nested refinement levels each with a grid resolution of 128^3 in addition to the top grid resolution of 128^3 both for the hydrodynamics and gravity. In total, we use 5767168 particles to solve the DM dynamics which yields an effective particle mass resolution of about 600 solar masses. We employ additional 18 refinement levels in the central 62 kpc region during the course of the simulations and resolve the Jeans length by 32 cells. Our refinement criteria are based on the gas overdensity and the particle mass resolution. The cells are marked for refinement if their density exceeds four times the cosmic mean density. Similarly, grid cells having DM densities above 0.0625 times $\rho_{DM} r^{\ell\alpha}$ are flagged for refinement where $r = 2$ is the refinement factor, ℓ is the refinement level, and $\alpha = -0.3$ makes the refinement super-Lagrangian. We further smooth the dark matter particles at refinement level 12 which is equivalent to 2 pc in physical units to avoid spurious numerical artifacts. The simulations are stopped after reaching the maximum refinement level.

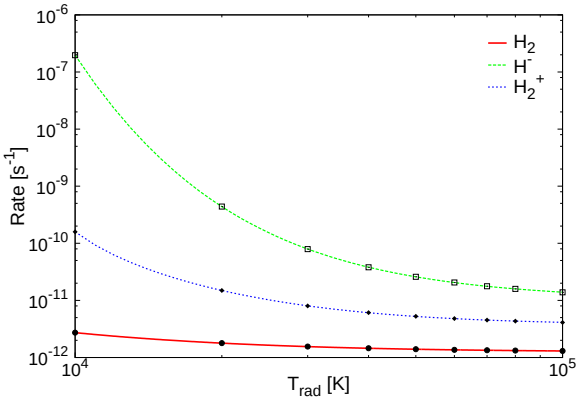

Figure 1. Photo-dissociation rates of H_2, H_2^+ & photo-detachment rate of H^- are plotted in this figure for various radiation temperatures between $T_{\rm rad} = 10^4 - 10^5$ K and J_{21}=1. Different line styles represent the fitting functions provided in table 1 and the symbols show the original data.

2.1 Chemical model

To follow the thermal and chemical evolution of the gas, we employ the publicly available package KROME[2] and its built-in ENZO patch (Grassi et al. 2014). The rate equations of H, H^+, He, He^+, He^{++}, e^-, H^-, H_2, H_2^+ are solved self-consistently along with the hydrodynamics in cosmological simulations. The processes involving deuterium species are ignored as they do not affect the findings of this work. We further presume here that a uniform isotropic background UV flux of various intensities below the Lyman limit (i.e. below 13.6 eV) in units of 10^{-21} erg cm^{-2} s^{-1} Hz^{-1} sr^{-1} is emitted by Pop II stars with black body radiation temperatures between $10^4 - 10^5$ K. As shown by Sugimura et al. (2014), such spectra effectively mimic the results from a realistic spectrum. In addition to this, we employ a cosmic X-ray background of various strengths (details are described below). Our chemical model is an extended form of Latif et al. (2014) with the addition of X-ray chemistry, updated rates and the H_2 cooling function for low densities by Glover & Abel (2008a). It further includes the photo-detachment of H^-, the photo-dissociation of H_2 and H_2^+, collisional dissociation, collisional induced emission, chemical cooling/heating from three-body reactions, cooling by collisional excitation, collisional ionization, radiative recombination and bremsstrahlung radiation (Grassi et al. 2014). For H_2 cooling, we used the escape probability given in Omukai (2000) which is based on the Sobolev approximation. The H_2 self-shielding fitting function by Wolcott-Green et al. (2011) is employed here.

Due to the smaller X-ray absorption cross-sections for hydrogen compared to the ionizing UV photons, X-rays can travel longer distances and build up a cosmic X-ray background (CXB). Following Glover & Brand (2003); Inayoshi & Omukai (2011a), we assume that the CXB has a power law spectrum with index of -1.5 and is given by

$$J_{\rm X}(\nu) = J_{\rm X,21} \times 10^{-21} \left(\frac{\nu}{\nu_0}\right)^{-1.5} \ {\rm erg\ cm^{-2}\ s^{-1}\ Hz^{-1}\ sr^{-1}} \qquad (5)$$

[1] http://enzo-project.org/, changeset:48de94f882d8

[2] www.kromepackage.org, changeset:4674be5

where $h\nu_0$=1 keV and $J_{X,21}$ is CXB flux in units of 10^{-21} erg cm^{-2} s^{-1} Hz^{-1} sr^{-1}. We also consider both primary and secondary ionization of H and He atoms. We ignore the contribution from the secondary ionization of HeII which is negligible in our case as also found in the previous studies (Shull & van Steenberg 1985). For the cosmic X-ray background, we consider photons between 2-10 keV as low energy X-ray photons are absorbed locally (Haiman et al. 1997). Further details about the implementation of X-ray physics, photo-chemistry and reactions rates are provided in the appendix.

3 MAIN RESULTS

3.1 Results from one-zone models

We have computed the photo-dissociation rates of H_2, H_2^+ as well as the photo-detachment of H^- which depend on the adapted radiation spectra and play a key role in determining the J_{21}^{crit}. These rates for $T_{rad} = 10^4 - 10^5$ K are not available in the literature. Therefore, we provide the fitting functions which are listed in table 1 and also shown in figure 1, see the appendix for detailed derivations (also see Fig. 4 in Omukai et al. (2008)). It is noted that the H^- photo-detachment reaction varies by about 3 orders of magnitude for $T_{rad} = 10^4 - 2\times10^4$ K and its dependence becomes very weak between $T_{rad} = 3\times10^4 - 10^5$ K. The H_2 photo-dissociation reaction varies by a factor of a few between $T_{rad} = 10^4 - 10^5$ K. The same is the case for H_2^+ photo-dissociation reaction.

To verify our chemical model described in the above section, we have performed a number of one-zone tests and show some representative cases here. For the one-zone test, we took the initial gas temperature of 160 K, an initial gas density of 0.1 cm^{-3} and initial abundances of the species of $e^- = 2\times10^{-4}$ and $H_2 = 2\times10^{-6}$, same as in Inayoshi & Omukai (2011a). Figure 2 depicts the thermal evolution and the abundances of H^-, H_2 and e^- for $T_{rad} = 2\times10^4$ K. It is found that with increasing strength of the impinging radiation field the thermal evolution splits into two distinct tracks, the H_2 and the atomic line cooling tracks. This trend is also evident in the abundance of H_2 where in the former case it reaches the universal abundance (i.e. 10^{-3}) while for the latter case, it remains a few orders of magnitude lower. This bifurcation defines the critical value of the incident flux which is found to be $J_{21}^{crit} = 300$ for a radiation spectrum of 2×10^4 K. This is an order of magnitude higher compared to the case of $T_{rad} = 10^4$ K. For the higher radiation temperature, the value of J_{21}^{crit} does not increase much as evident from the reaction rates discussed above and also clear from figure 9.

In comparison with previous studies, our results in general are consistent with Shang et al. (2010) and Sugimura et al. (2014). However, the value of J_{21}^{crit} is a factor of a few lower from Sugimura et al. (2014). This difference mainly arises by considering the effect of dissociative tunneling for the collisional dissociation of H_2 (Martin et al. 1996a). It reduces the value of J_{21}^{crit} by a factor of 3. A similar effect was also observed by Latif et al. (2014).

Motivated by the work of Inayoshi & Omukai (2011a) who found that the presence of a strong CXB further elevates the value of J_{21}^{crit}, we have performed one-zone calculations including the X-ray background feedback. In figure 3, we show the impact of X-ray ionization for a CXB strength of $J_{X,21} = 0.1$ and $T_{rad} = 2\times10^4$ K. It is found that for $J_{X,21} < 0.01$ the impact of X-rays is negligible and starts to become important around $J_{X,21} = 0.1$ where gas is instantly heated to 8000 K, the cooling threshold for the Lyman alpha line. A similar effect of X-ray heating has been observed in one-zone calculations as well as in 3D simulations (Wolfire et al. 1995; Inayoshi & Omukai 2011b; Hummel et al. 2014). It has been found that X-ray heating is only important at low densities < 1 cm^{-3} and the heating rate is of the order of 10^{-4} erg s^{-1} g^{-1} which is a factor of 10 higher than other heating sources such as compressional heating. For a given intensity of J_{21}, it boosts the formation of H_2 and cools the gas down to a few hundred K. Consequently, it elevates the critical threshold of the UV flux by a factor of 5. A similar result was found by Inayoshi & Omukai (2011a) but in their case the X-ray heating becomes already important for $J_{X,21} = 0.01$ as they used the X-ray photo-ionization cross-section of He from Osterbrock (1989). We here use the recent cross-section by Verner et al. (1996) which is three orders of magnitude smaller and requires a higher value of $J_{X,21}$ to elevate the value of J_{21}^{crit}.

3.2 Results from 3D simulations

In all, we have performed 25 simulations to compute the value of J_{21}^{crit} for the realistic Pop II spectra. We further compute the dependence of J_{21}^{crit} on radiation spectra, on the impact of X-ray ionization, and on variations from halo to halo. We have selected three primordial halos of a few times 10^7 M$_\odot$ forming at $z > 10$ and varied the strength of the incident flux for a given radiation temperature.

3.3 Impact of radiation spectra

We assessed the dependence of J_{21}^{crit} on radiation spectra by selecting three representative radiation spectra i.e. $T_{rad} = 2\times10^4, 4\times10^4, 8\times10^4$ K for the halo A. In figure 4, we show the radial profiles of gas density, temperature, the H_2 abundance and electron fraction. In the presence of a strong UV flux, initially the H_2 cooling remains suppressed until the halo reaches its virial temperature and a density of about $10 - 100$ cm^{-3}. Such trend is observed for all values of J_{21} irrespective of the radiation temperature.

As the halo begins to collapse the H_2 abundance increases and further gets boosted in the weaker UV flux cases. For the stronger radiation fields, the formation of H_2 gets delayed to higher densities until the H_2 abundance reaches above 10^{-4} in the center of the halo and the H_2 self-shielding becomes effective. By further increasing the strength of UV flux, the thermal evolution becomes isothermal and the formation of H_2 remains suppressed in the presence of intense radiation fields. The H_2 abundance in such cases is $< 10^{-7}$ (well above the universal abundance, i.e. 10^{-3}) and the central temperature of the halo decreases down to about 1000 K. The degree of ionization in the core of halos is higher for higher central temperatures. The density profiles for the atomic and H_2 cooling are significantly different from each other because of the different thermal evolutions. A similar trend is observed for all the radiation spectra studied here. The values of J_{21}^{crit} for $T_{rad} = 2\times10^4,\ 4\times10^4$ & 8×10^4 K are $2\times10^4, 3\times10^4$ & 3×10^4, respectively.

Table 1. The fitting functions for the photo-dissociation of H_2, H_2^+ and the photo-detachment of H^-. They are valid for $T_{\rm rad} = 10^4 - 10^5$ K.

Coefficients	$k_{H_2}[s^{-1}]$	$k_{H^-}[s^{-1}]$	$k_{H_2^+}[s^{-1}]$
	$\mathrm{dex}[(a+bT_{\rm rad}+cT_{\rm rad}^2)^{-1}-d]$	$\mathrm{dex}[(a+bT_{\rm rad})^{-1/c}-d]$	$(-a+bT_{\rm rad})^{-1/c}+d$
a	1.1735×10^{-1}	9.08944×10^{-2}	3.83012×10^{6}
b	2.4958×10^{-4}	3.27940×10^{-5}	5.06440×10^{2}
c	3.4856×10^{-9}	5.98490×10^{-1}	6.20988×10^{-1}
d	1.1902×10^{1}	1.09867×10^{1}	3.68778×10^{-12}

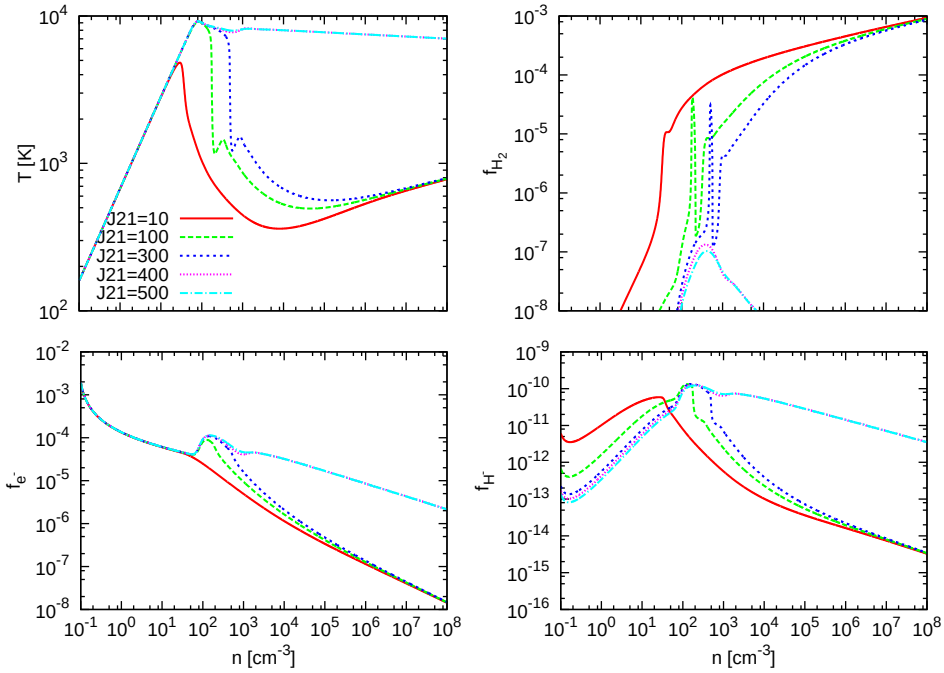

Figure 2. One-zone plot for $T_{\rm rad} = 2\times10^4$ K. The temperature and the abundances of H_2, e^- and H^- are plotted against the number density for various strengths of a background UV flux.

For $T_{\rm rad} \geq 2\times10^4$ K, the variations in $J_{21}^{\rm crit}$ are not significant and the $J_{21}^{\rm crit}$ becomes constant for radiation temperatures above 3×10^4 K. Overall, the value of $J_{21}^{\rm crit}$ is about two orders of magnitude larger than in the one-zone calculations. The differences between the one-zone and 3D simulations are also observed in Shang et al. (2010) & Latif et al. (2014), and come from the inability of one-zone models to simulate shocks and hydrodynamical effects. These processes significantly enhance the ionization degree in realistic simulations, and stimulate the formation of H_2. As a results, a stronger radiation field is required to balance this effect.

3.4 Variations from halo to halo

To study the variations of $J_{21}^{\rm crit}$ from halo to halo, we selected three distinct halos and determined $J_{21}^{\rm crit}$ by varying the strength of the incident UV flux. For this purpose, we fixed the temperature of radiation spectra to $T_{\rm rad} = 2\times10^4$ K. This choice is justified from the fact that the critical value only weakly depends on the radiation spectrum above this value as found in the previous section. The thermal evolution, the density profiles, the H_2 abundances and electron fractions for these halos are shown in figure 5. It is noted that by increasing the intensity of the UV field, the formation of H_2 remains suppressed and thermal becomes isothermal for $J_{21}^{\rm crit}$ few times 10^4. The values of $J_{21}^{\rm crit}$ for the simulated halos are $2\times10^4, 4\times10^4$ & 5×10^4 and also listed in table 2. These variations from halo to halo are within a factor of 3 and are due to the differences in the density structures, spins, formation histories and the collapse redshifts. A similar dependence of $J_{21}^{\rm crit}$ on the halo properties was observed in previous studies (Shang et al. 2010; Latif et al. 2014).

In figure 6, we show the time evolution of the density, temperature, H_2 and e^- fractions for two representative cases of atomic and molecular hydrogen cooling. They are shown for the halo A and radiation spectra of $T_{\rm rad} = 2\times10^4$ K. It is found that at low densities the formation of H_2 remains suppressed and gas is heated up to $\geq 10^4$ K which corresponds to the virial temperature of the halo. The halo starts to virialize at $z \sim 12$. For $J_{21} = 1000$, the significant amount of H_2 forms at densities above 10^4 cm^{-3} and lowers the temperature of the halo down to a few hundred K. While for $J_{21} = 4\times10^4$, the formation of H_2 remains suppressed and leads to an isothermal collapse.

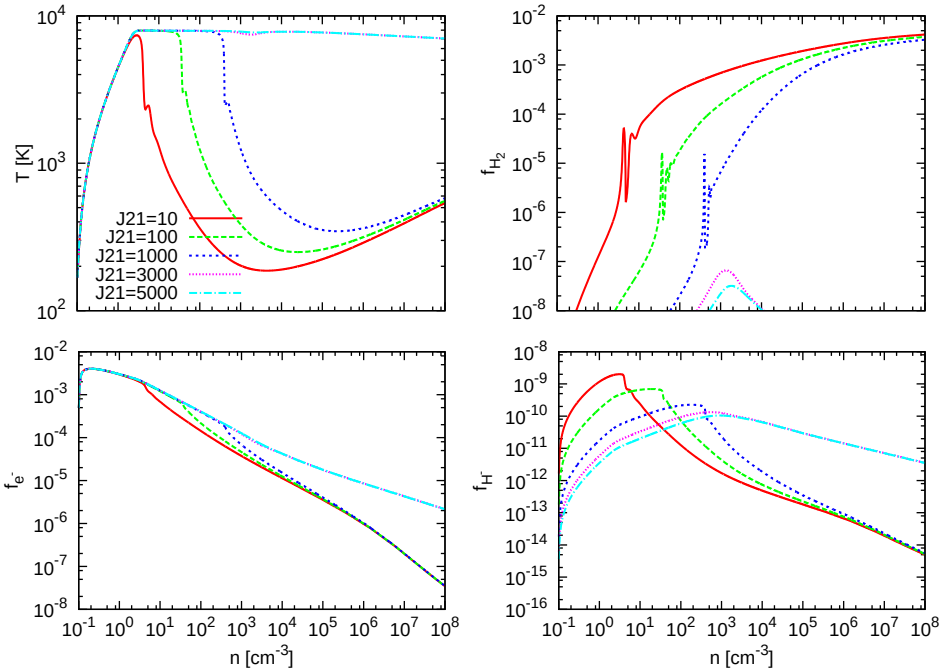

Figure 3. Same as figure 2 for the X-ray flux of $J_{X,21} = 0.1$.

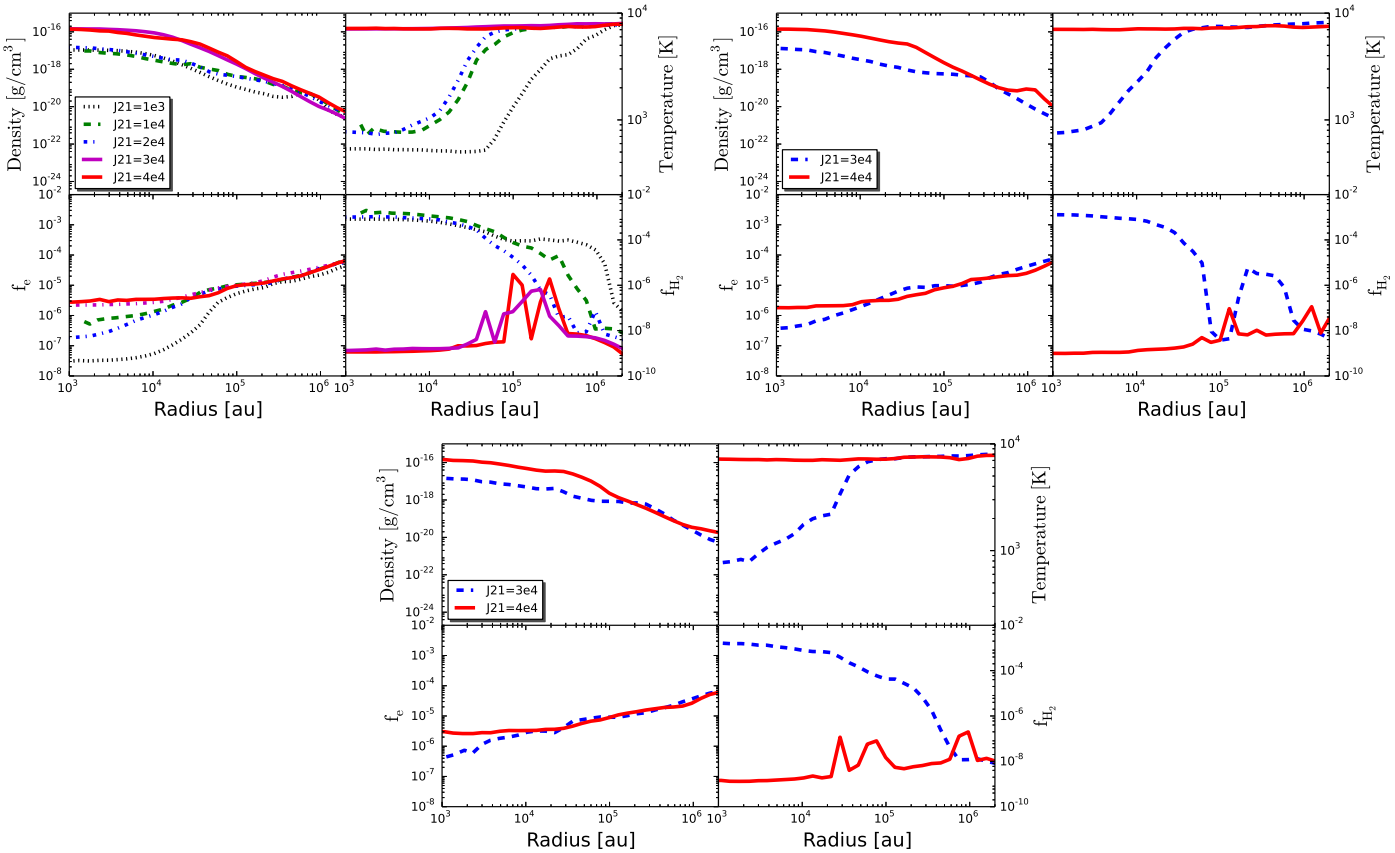

Figure 4. Spherically averaged and radially binned profiles of temperature, density, H_2 and e^- fractions computed for the peak density in the simulations are plotted for the halo A. The top panels represent $T_{\rm rad} = 2.0 \times 10^4$ K (left) $T_{\rm rad} = 4.0 \times 10^4$ K (right) and the bottom panel $T_{\rm rad} = 8.0 \times 10^4$ K. Each line style depicts the value of J_{21} as mentioned in the legend.

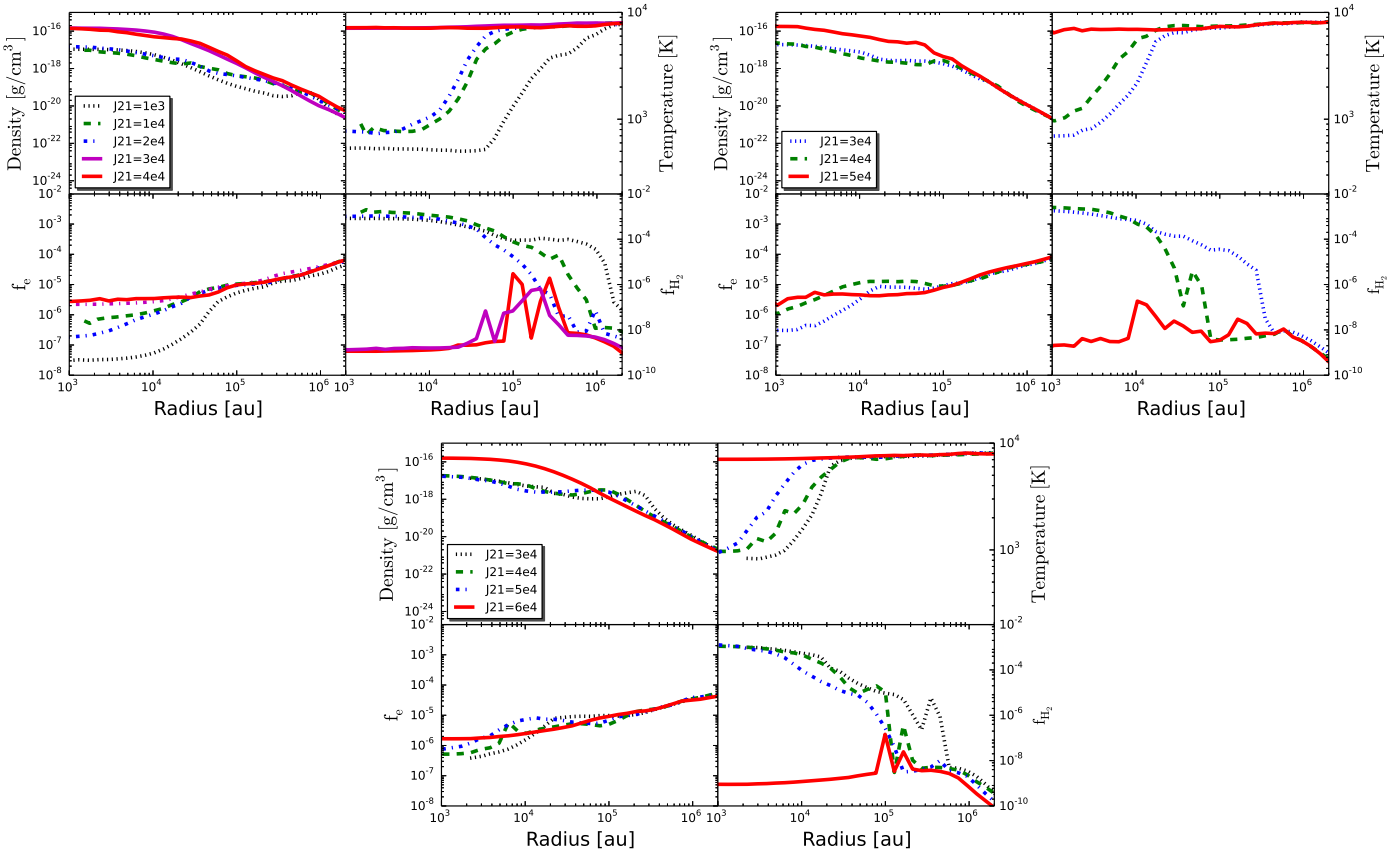

Figure 5. Spherically averaged and radially binned profiles of temperature, density, H_2 and e^- fractions computed for the peak density in the simulations are plotted for $T_{\rm rad} = 2.0 \times 10^4$ K. The top panels represent halos A & B (left to right) and the bottom panel halo C. Each line style depicts the value of J_{21} as mentioned in the legend. The collapse redshifts of these halos are listed in table 2

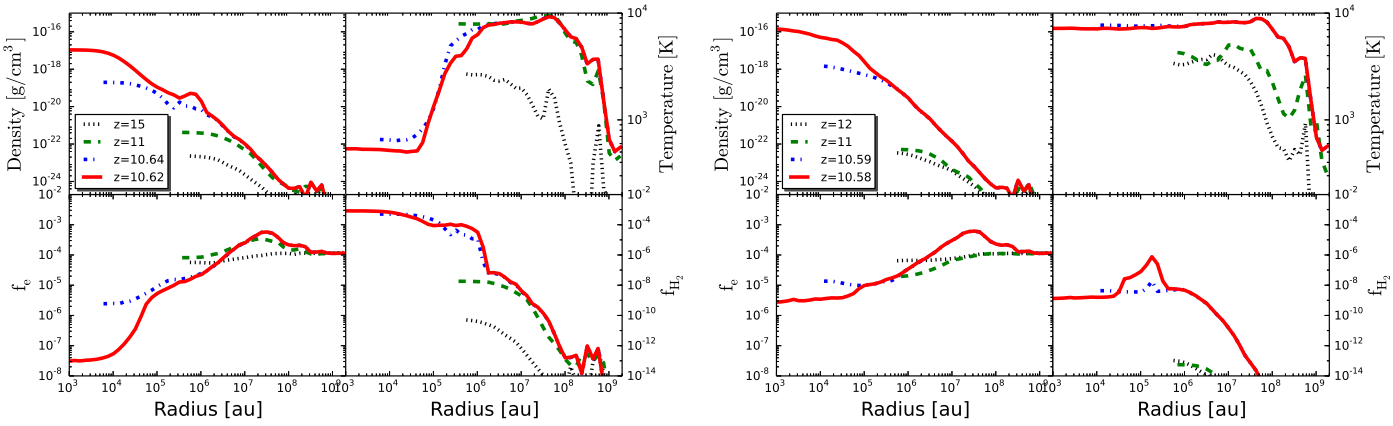

Figure 6. Time evolution of spherically averaged and radially binned profiles of temperature, density, H_2 and e^- fractions is shown for the halo A and $T_{\rm rad} = 2.0 \times 10^4$ K. Each line style represents a different redshift as shown in the legend. The left panel shows the H_2 cooling case and the right panel depicts atomic cooling case.

3.5 Impact of X-ray ionization

We investigated the impact of X-ray ionization on three different halos already exposed to a strong UV flux. To achieve this goal, we selected the UV fluxes above the critical value to see the potential influence of X-ray ionization in enhancing $J_{21}^{\rm crit}$ for a fixed radiation temperature of $T_{\rm rad} = 2 \times 10^4$ K. An X-ray background flux of strengths $J_{X,21} = 0.01$ & 0.1 was turned on at redshift 30. In figure 7, we show the profiles of density, temperature, the H_2 and e^- fractions. They are very similar to the isothermal cases except for halo A. The value of $J_{21}^{\rm crit}$ is elevated by a factor of two for halo A from 2×10^4 to 4×10^4 for $J_{X,21} = 0.1$ while for the other two halos the impact of X-ray ionization is negligible and $J_{21}^{\rm crit}$ remains

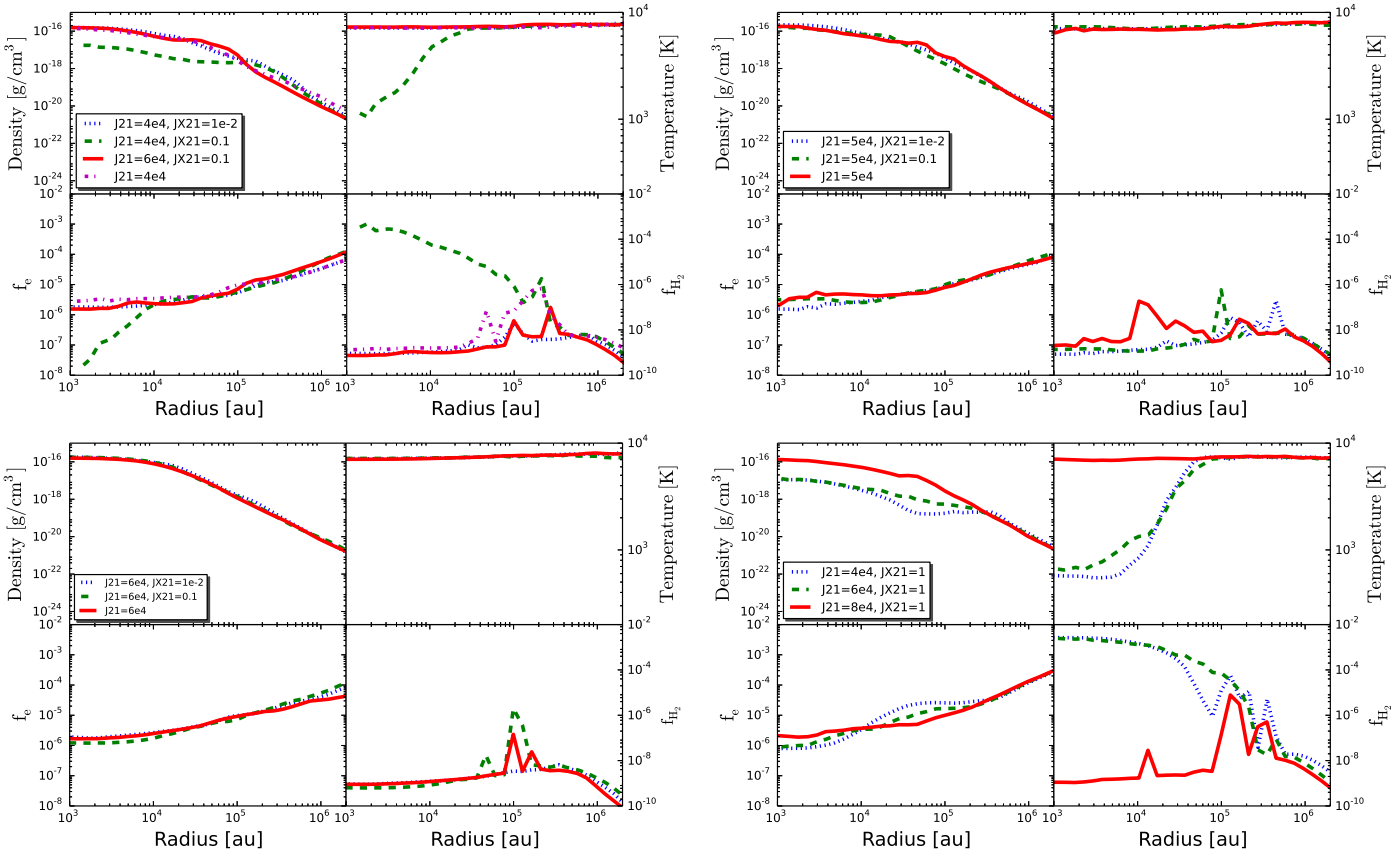

Figure 7. Spherically averaged and radially binned profiles of temperature, density, H_2 and e^- fractions computed for the peak density in the simulations are plotted for $T_{\rm rad} = 2.0 \times 10^4$ K and also include X-ray background. The top panels represent halos A & B (left to right) and the bottom left panel halo C while the right panel for halo A with higher X-ray flux. Each line style depicts the value of J_{21} as mentioned in the legend.

Table 2. Properties of the simulated halos for $J_{21}^{\rm crit}$ are listed here.

Model No	Mass $M_\odot$	Redshift z	$J_{21}^{\rm crit}$ $T_{\rm rad} = 2 \times 10^4$ K	$J_{\rm X,21}^{crit}$ in units of $J_{\rm X,21}$	spin parameter λ
A	5.6×10^7	10.59	20000	40000	0.034
B	4.06×10^7	13.23	40000	40000	0.02
C	3.25×10^7	11.13	50000	50000	0.03

unchanged. For even higher strength of $J_{\rm X,21} = 1$, the value of $J_{21}^{\rm crit}$ is enhanced by a factor of four compared to $J_{\rm X,21} = 0.01$. This comes from the fact that X-ray heating at low densities enhances the degree of ionization which further boosts the H_2 fraction consequently a higher value of UV flux is required to quench the formation of molecular hydrogen. For high values of $J_{\rm X,21}$, our results are thus roughly consistent with the trend $J_{21}^{\rm crit} \sim J_{X,21}^{1/2}$ suggested by Inayoshi & Omukai (2011b), even though the influence is reduced for more moderate values.

The observations of the unresolved cosmic X-ray background at 0.2-8 keV from the Chandra Deep Fields found an intensity value of $J_{\rm X,21} = 10^{-5}$ (Hickox & Markevitch 2006). Here, we studied rather extreme cases a few orders of magnitude above the expected CXB (Salvaterra et al. 2007; Ciardi et al. 2010) but the impact is still weak and is within the range of variations from halo to halo. In one-zone calculations, small variations in the degree of ionization are significant to elevate the critical value by a factor of few. On the other hand, in 3D simulations the effect of X-ray ionization is comparable to the presence of strong UV field and accretion shocks which already boost the degree of ionization. Therefore, overall the impact of X-ray ionization on $J_{21}^{\rm crit}$ is negligible for most cases studied here.

So far, we have assumed that the X-ray background is emitted from the first galaxies. In fact, the X-ray luminosity in 2-10 keV range is related to the star formation rate (Glover & Brand 2003) as:

$$L_{\rm X} = 6 \times 10^{39} \left(\frac{SFR}{1\ M_\odot/yr} \right) \ {\rm erg\ s^{-1}} \qquad (6)$$

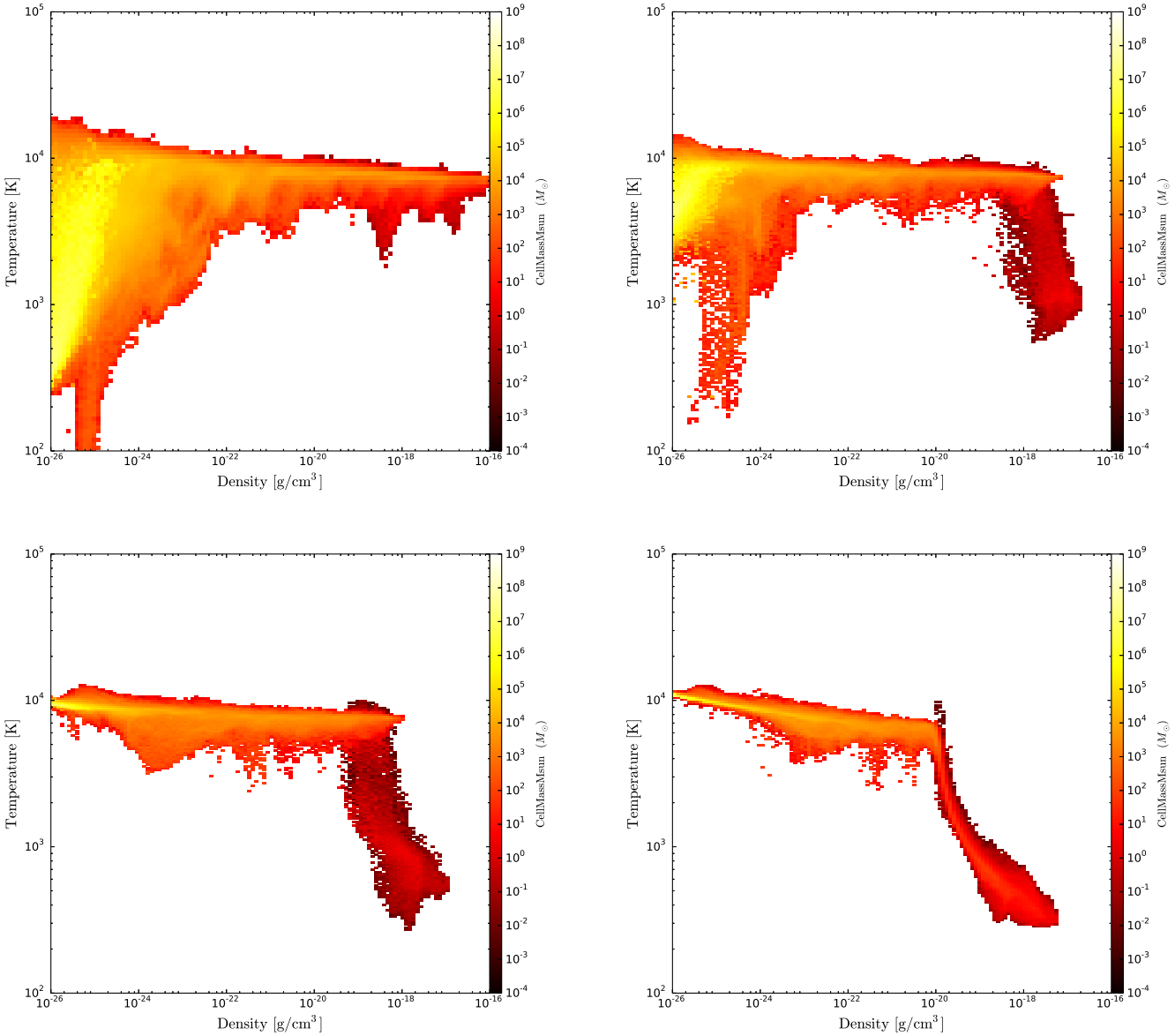

Figure 8. The phase plots (temperature verses density) of the halo A for $T_{\rm rad} = 2\times10^4$ K and various value of $J_{\rm X,21}$. The top two panels represent $J_{\rm X,21} = 0.01$ & $J_{\rm X,21} = 0.1$ while the bottom two panels represent $J_{\rm X,21} = 1$ & $J_{\rm X,21} = 10$ from left to right, respectively.

where SFR is the star formation rate. For a given SFR and distance from the source, the X-ray flux can be computed as (Inayoshi & Omukai 2011b):

$$J_{\rm X,21} = 4.5\times10^{-3}\left(\frac{d}{10\ kpc}\right)^{-2}\left(\frac{SFR}{20\ M_\odot yr^{-1}}\right) \quad (7)$$

This empirical relation suggests that for SFRs of 20-100 $M_\odot\ yr^{-1}$, the X-ray flux at a distance of 10 kpc from the source varies from a few times $10^{-3} - 10^{-2}$ in units of $J_{X,21}$. In the case of a nearby accreting supermassive black hole of 10^9 $M_\odot$, the X-ray luminosity is about 10^{44} erg s^{-1} for a peak emission around 2 keV. This yields an X-ray flux of strength $J_{\rm X,21} = 3$ at a distance of 10 kpc. These estimates suggest that the values of the X-ray background investigated here are a few orders of magnitude larger than the CXB. However, the cases investigated here may occur in the vicinity of a supermassive black hole which would therefore tend to suppress the formation of additional nearby black holes.

Recently, Hummel et al. (2014) have investigated the impact of only X-ray feedback (no UV flux) on a minihalo of 10^5 $M_\odot$ at $z = 25$ and found that X-ray feedback has a dual effect. X-ray heating is dominant at low densities, i.e. < 1 cm^{-3} and the cooling ability of the gas gets enhanced above 10^2 cm^{-3} due to the higher degree of ionization. They found that X-ray feedback has a so-called Goldilocks range of the X-ray background for which it promotes star formation while for the higher strengths it suppresses the collapse. This Goldilocks range of CXB starts around $J_{\rm X,21} = 0.1$ and complete blowout occurs for $J_{\rm X,21} = 10$ where it completely suppresses the collapse of a minihalo.

The halos studied here are about an order of magnitude more massive than the minihalos therefore the impact of X-rays is expected to be less severe. In figure 8, we show the impact of X-ray heating and ionization for various strengths of $J_{X,21}$ from 0.01-10. The temperature of the cold component of the gas scales with the strength of X-ray feedback. It is noted that for the highest strength of $J_{X,21}$ the gas is heated above 10^4 K and cools by Lyman alpha radiation. X-rays increase the degree of ionization, which consequently promotes the cold component of the gas at higher densities. This is particularly notable for $J_{X,21} = 10$ for which the central temperature of the halo reaches about 300 K due to the higher H_2 abundance. In a nutshell, for the X-ray background to be effective to raise the critical threshold for UV flux it should have at least a strength of $J_{X,21} \geq 0.1$.

We further explored the influence of X-ray feedback of strength $J_{X,21} = 100$ for the halo A. We found that the collapse of the halo is delayed by $\Delta z = 1$, i.e., 50 million years, but it is not disrupted. Therefore, blowout of massive primordial halos is very unlikely and may occur only for very extreme X-ray feedback of strength higher than investigated here. It is noted that such an extreme strength of the X-ray background can only be achieved at a distance of 1 kpc from an accreting supermassive black holes of a billion solar masses. The impact of X-ray feedback on the collapse dynamics and subsequent star formation in massive hales should be investigated in future studies via 3D simulations.

3.6 Implications for the formation of DCBHs

It is a prerequisite for DCBHs that the formation of H_2 remains suppressed in their "potential embryos" atomic cooling halos. Quenching the H_2 formation mandates the presence of an intense UV flux which can be achieved in the close proximity (about 10 kpc) of a star forming galaxy (Dijkstra et al. 2008; Agarwal et al. 2012; Dijkstra et al. 2014). It is likely that such a flux is provided by Pop II stars which are abundant enough to illuminate the number of DCBHs sites comparable with the observed number density of high redshift quasars at $z > 6$ (Dijkstra et al. 2014; Latif et al. 2014).

The accurate determination of $J_{21}^{\rm crit}$ for realistic Pop II spectra is highly relevant to predict the sites of DCBHs and to test the feasibility of the direct collapse scenario. Agarwal et al. (2012), and Dijkstra et al. (2014) have estimated the abundance of DCBHs from semi-analytical calculations along with N-body and Monte-Carlo simulations. They assumed that DCBHs are formed in the atomic cooling halos irradiated by $J_{21} > J_{21}^{\rm crit}$ by taking $J_{21}^{\rm crit} = 30$ and $J_{21}^{\rm crit} = 300$ respectively. Their predictions lead to the DCBHs abundances of 3×10^{-3}/cMpc^3 and 10^{-7}/cMpc^3 (respectively) higher than the observed SMBHs number density of 10^{-9}/cMpc^3 (Fan 2003; Venemans et al. 2013). Recently, Sugimura et al. (2014) extrapolated the estimates of Dijkstra et al. (2014) by using their one-zone estimates of $J_{21}^{\rm crit} = 1400$ and found that number density of DCBHs drops to 10^{-10}/cMpc^3 at $z = 10$.

In figure 9, we summarize our estimates of $J_{21}^{\rm crit}$ from one-zone, 3D simulations, variations from halo to halo, dependence on the radiation spectra and from the impact of X-ray ionization. Our calculation of $J_{21}^{\rm crit}$ for the realistic Pop II spectra suggest that $J_{21}^{\rm crit}$ varies from 20,000-50,000. Extrapolating the results of Dijkstra et al. (2014) with $J_{21}^{\rm crit} = 40,000$

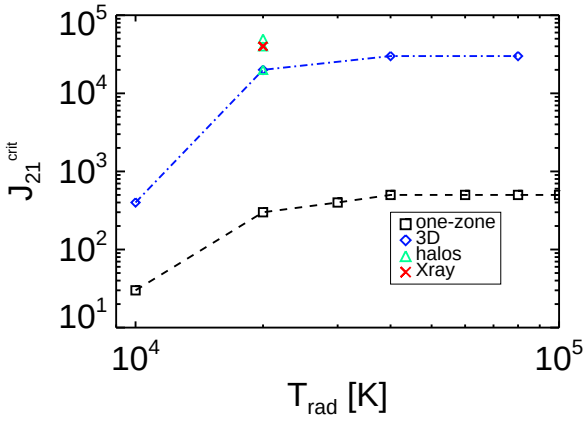

Figure 9. Summary plot. In this figure, we show the results from one-zone model and 3D simulations performed to compute the variations from halo to halo, dependence on the radiation spectra & the impact of X-ray ionization.

the number density of DCBH sites drops about 5 orders of magnitude below the observed quasars density. Our results suggest that direct collapse black holes forming through an isothermal may be even more rare than previously perceived. However, as recently shown by Latif et al. (2014), the formation of massive objects is still conceivable for moderate amounts of H_2 cooling, implying that this formation channel deserves further exploration in the future.

4 DISCUSSION

The prime requisitions for the formation of isothermal direct collapse black holes are that the hosting halos must be of primordial composition and remain H_2 free. The first condition can be accomplished in the massive halos forming from primordial gas composition at $z = 15$. The suppression of H_2 demands the presence of a strong UV flux during their formation. Such flux is conceived to be produced by the second generation of stars at earlier cosmic epochs. In this study, we compute the critical value of UV flux necessary for the formation of direct collapse black holes for the realistic Pop II spectra by preforming high resolution cosmological simulations. We further compute the dependence of $J_{21}^{\rm crit}$ on the radiation spectra, study the impact of X-ray ionization and variations for halo to halo.

In these simulations, we followed the initial collapse of DM halos to high densities from which stars and black holes may subsequently form. The masses of these stars depend on the thermal properties of the host halos and massive to supermassive stars are expected to form. Particularly, for the isothermal collapse, a supermassive star of 10^5 $M_\odot$ is expected to form which will later collapse into a BH. The X-ray feedback from such a direct collapse BH may trigger in-situ star formation in about 0.5 Myrs after its formation (Aykutalp et al. 2014). The local star formation may induce metal enrichment and consequently change the thermal structure of the gas, and also the gas dynamics due to the injection of turbulence energy. Overall, we do not expect star formation to inhibit black hole growth, and in fact the

injected turbulent energy helps to transfer the angular momentum and maintain the accretion rates (Wutschik et al. 2013).

Our findings suggest that the value of $J_{21}^{\rm crit}$ for realistic Pop II spectra is a few times 10^4. For the simulated halos, it varies from $2\times10^4 - 5\times10^4$ and also weakly depends on the radiation spectra in the range $T_{\rm rad} = 2\times10^4 - 10^5$ K. We further found that the impact of X-ray ionization for the halos irradiated by strong UV flux is negligible for $J_{\rm X,21} \leq 0.1$ and does not elevate the $J_{21}^{\rm crit}$ for UV flux in contrary to the previous studies. For $J_{\rm X,21} > 0.1$ it does have a factor of a few effect on $J_{21}^{\rm crit}$. However, we noted that in one of the simulated halos it changed the $J_{21}^{\rm crit}$ from $2\times10^4-4\times10^4$. This increase is within the expected scatter in the values of $J_{21}^{\rm crit}$. The results from 3D simulations differ by about two orders of magnitude from one-zone calculations due to the inability of one-zone models to simulate shocks, collapse dynamics and hydrodynamical effects as found in the previous studies (Shang et al. 2010; Latif et al. 2014). In comparison with earlier works, our one-zone results differ by a factor of 3 from Sugimura et al. (2014). This difference arises by considering the dissociative tunneling effect in the collisional dissociation of H_2. For very strong X-ray fluxes, we can roughly confirm their trend of $J_{21}^{\rm crit} \sim J_{X,21}^{1/2}$, even though such cases may occur in the presence of a supermassive black hole.

For this study, we have presumed that the halo is illuminated by an isotropic background UV flux of constant strength. It is likely that a direct collapse halo is irradiated by multiple sources, in such case the expected background is approximately isotropic as seen in the simulations of Agarwal et al. (2014). However, the recent work by Regan et al. (2014) shows that in the case of an anisotropic single source the value of $J_{21}^{\rm crit}$ is few times 10^3 and almost consistent with our results. It may also be noted that Regan et al. (2014) consider a monochromatic source of Lyman-Werner radiation and ignore other dissociation channels particularly H^-. We further suggest that our estimates of $J_{21}^{\rm crit}$ are also valid both for pop III stars with radiation temperature of 10^5 K. We have not considered here the impact of ionizing UV radiation which further enhances the degree of ionization and elevates the value of $J_{21}^{\rm crit}$ (Johnson et al. 2014). It should also be noted that strong dissipation of magnetic energy into thermal energy may reduce the value of $J_{21}^{\rm crit}$ (Sethi et al. 2010; Van Borm & Spaans 2013). Once the gas is dense enough about 10^4 cm^{-3} and above temperature of few thousand K then collisional dissociation becomes effective leading to the destruction of H_2 (Inayoshi & Omukai 2012).

The higher value of $J_{21}^{\rm crit}$ (i.e. 10^4) found from this work suggests that complete photo-dissociation sites are very rare and less abundant than the number of quasars observed at $z = 10$. However, as found in Latif et al. (2014) even in the cases where H_2 is not completely dissociated still massive objects of 10^4 $M_\odot$ may form provided that accretion rates remain higher than 0.1 $M_\odot$ yr^{-1}. For such accretion rates, the feedback from the protostar remains suppressed and accretion can proceed for longer time scales (Hosokawa et al. 2013; Schleicher et al. 2013). Even if fragmentation occurs at high densities inside the disk due to the H^- or dust cooling, clumps may merge in the center on a shorter time scale than the Kelvin-Helmholtz time scale (Inayoshi & Haiman 2014). Such seeds are still an order of magnitude more massive than remnants of Pop III stars or stellar cluster. We argue here that such sites are strong contenders to the scarce isothermal collapse.

Our study does not capture the subtle time dependent effects of Pop II spectra such as spectral dependence on the age, metallicity and stellar mass function. Recent attempts to model these effects are in disagreement (Agarwal & Khochfar 2014; Sugimura et al. 2014), therefore further investigations in this direction are required. In the future, alternative channels for the formation of seed black holes should be explored to test their feasibility.

ACKNOWLEDGMENTS

The simulations described in this work were performed using the Enzo code, developed by the Laboratory for Computational Astrophysics at the University of California in San Diego (http://lca.ucsd.edu). We are grateful to Philipp Stancil and Bob Forrey for sharing the H^- cross-sections. We thank Kohei Inayoshi for his valuable feedback on X-ray physics. We also thank Daniele Galli for fruitful discussions on H_2 photodissociation. We acknowledge research funding by Deutsche Forschungsgemeinschaft (DFG) under grant SFB 963/1 (project A12) and computing time from HLRN under project nip00029. DRGS and SB thank the DFG for funding via the Schwerpunktprogram SPP 1573 "Physics of the Interstellar Medium" (grant SCHL 1964/1 – 1). TG acknowledges the Centre for Star and Planet Formation funded by the Danish National Research Foundation. The simulation results are analyzed using the visualization toolkit for astrophysical data YT (Turk et al. 2011).

REFERENCES

Abel T., Anninos P., Zhang Y., Norman M. L., 1997, New Astronomy, 2, 181
Agarwal B., Dalla Vecchia C., Johnson J. L., Khochfar S., Paardekooper J.-P., 2014, MNRAS, 443, 648
Agarwal B., Khochfar S., 2014, ArXiv e-prints:1407.4115
Agarwal B., Khochfar S., Johnson J. L., Neistein E., Dalla Vecchia C., Livio M., 2012, MNRAS, 425, 2854
Aldrovandi S. M. V., Pequignot D., 1973, A&A, 25, 137
Alvarez M. A., Wise J. H., Abel T., 2009, ApJ, 701, L133
Aykutalp A., Wise J. H., Spaans M., Meijerink R., 2014, ArXiv e-prints:1409.0543
Ball W. H., Tout C. A., Żytkow A. N., 2012, MNRAS, 421, 2713
Begelman M. C., 2010, MNRAS, 402, 673
Begelman M. C., Volonteri M., Rees M. J., 2006, MNRAS, 370, 289
Bovino S., Grassi T., Latif M. A., Schleicher D. R. G., 2013, MNRAS, 434, L36
Bovino S., Grassi T., Schleicher D. R. G., Latif M. A., 2014, ApJ, 790, L35
Bromm V., Loeb A., 2003, ApJ, 596, 34
Bryan G. L., Norman M. L., O'Shea B. W., Abel T., Wise J. H., Turk M. J., Reynolds D. R., Collins D. C., So G. C., Zhao F., Cen R., Li Y., The Enzo Collaboration 2014, ApJS, 211, 19

Capitelli M., Coppola C. M., Diomede P., Longo S., 2007, A&A, 470, 811
Cazaux S., Spaans M., 2009, A&A, 496, 365
Cen R., 1992, ApJS, 78, 341
Ciardi B., Salvaterra R., Di Matteo T., 2010, MNRAS, 401, 2635
Colella P., Woodward P. R., 1984, Journal of Computational Physics, 54, 174
Coppola C. M., Longo S., Capitelli M., Palla F., Galli D., 2011, ApJS, 193, 7
Corrigan S. J. B., 1965, JCP, 43, 4381
Dalgarno A., Lepp S., 1987, in Vardya M. S., Tarafdar S. P., eds, Astrochemistry Vol. 120 of IAU Symposium, Chemistry in the early universe. pp 109–118
de Jong T., 1972, A&A, 20, 263
Devecchi B., Volonteri M., 2009, ApJ, 694, 302
Dijkstra M., Ferrara A., Mesinger A., 2014, MNRAS, 442, 2036
Dijkstra M., Haiman Z., Mesinger A., Wyithe J. S. B., 2008, MNRAS, 391, 1961
Dopcke G., Glover S. C. O., Clark P. C., Klessen R. S., 2013, ApJ, 766, 103
Dunn G. H., 1968, Physical Review, 172, 1
Fan X., 2003, in Bulletin of the American Astronomical Society Vol. 35 of Bulletin of the American Astronomical Society, The Most Distant Quasars: Probing the End of Cosmic Dark Ages. pp 1415–+
Fan X., Strauss M. A., Richards G. T., Hennawi J. F., Becker R. H., White R. L., Diamond-Stanic A. M., 2006, AJ, 131, 1203
Fan X., Strauss M. A., Schneider D. P., Becker R. H., White R. L., Haiman Z., Gregg M., 2003, AJ, 125, 1649
Ferland G. J., Peterson B. M., Horne K., Welsh W. F., Nahar S. N., 1992, ApJ, 387, 95
Ferrara A., Salvadori S., Yue B., Schleicher D., 2014, MNRAS, 443, 2410
Forrey R. C., 2013, ApJL, 773, L25
Furlanetto S. R., Stoever S. J., 2010, MNRAS, 404, 1869
Glover S. C. O., Abel T., 2008a, MNRAS, 388, 1627
Glover S. C. O., Abel T., 2008b, MNRAS, 388, 1627
Glover S. C. O., Brand P. W. J. L., 2003, MNRAS, 340, 210
Glover S. C. O., Jappsen A.-K., 2007, ApJ, 666, 1
Grassi T., Bovino S., Schleicher D. R. G., Prieto J., Seifried D., Simoncini E., Gianturco F. A., 2014, MNRAS, 439, 2386
Haiman Z., 2004, ApJ, 613, 36
Haiman Z., 2012, ArXiv e-prints-1203.6075
Haiman Z., Rees M. J., Loeb A., 1997, ApJ, 476, 458
Hickox R. C., Markevitch M., 2006, ApJ, 645, 95
Hirano S., Hosokawa T., Yoshida N., Umeda H., Omukai K., Chiaki G., Yorke H. W., 2014, ApJ, 781, 60
Hosokawa T., Yorke H. W., Inayoshi K., Omukai K., Yoshida N., 2013, ApJ, 778, 178
Hummel J. A., Stacy A., Jeon M., Oliveri A., Bromm V., 2014, ArXiv e-prints:1407.1847
Inayoshi K., Haiman Z., 2014, ArXiv e-prints:1406.5058
Inayoshi K., Omukai K., 2011a, MNRAS, 416, 2748
Inayoshi K., Omukai K., 2011b, MNRAS, 416, 2748
Inayoshi K., Omukai K., 2012, MNRAS, 422, 2539
Janev R. K., Langer W. D., Evans K., 1987, Elementary processes in Hydrogen-Helium plasmas - Cross sections and reaction rate coefficients
Jarosik N., Bennett C. L., Dunkley J., Gold B., Greason M. R., Halpern M., Hill R. S., Hinshaw G., 2011, ApJS, 192, 14
Jeon M., Pawlik A. H., Bromm V., Milosavljević M., 2014, MNRAS, 440, 3778
Johnson J. L., Bromm V., 2007, MNRAS, 374, 1557
Johnson J. L., Whalen D. J., Agarwal B., Paardekooper J.-P., Khochfar S., 2014, ArXiv e-prints:1405.2081
Karpas Z., Anicich V., Huntress W. T., 1979, JCP, 70, 2877
Kreckel H., Bruhns H., Čížek M., Glover S. C. O., Miller K. A., Urbain X., Savin D. W., 2010, Science, 329, 69
Kuhlen M., Madau P., 2005, MNRAS, 363, 1069
Latif M. A., Bovino S., Van Borm C., Grassi T., Schleicher D. R. G., Spaans M., 2014, MNRAS, 443, 1979
Latif M. A., Niemeyer J. C., Schleicher D. R. G., 2014, MNRAS, 440, 2969
Latif M. A., Schleicher D. R. G., Bovino S., Grassi T., Spaans M., 2014, ApJ, 792, 78
Latif M. A., Schleicher D. R. G., Schmidt W., 2014, MNRAS, 440, 1551
Latif M. A., Schleicher D. R. G., Schmidt W., Niemeyer J., 2013a, MNRAS, 433, 1607
Latif M. A., Schleicher D. R. G., Schmidt W., Niemeyer J., 2013b, MNRAS, 430, 588
Latif M. A., Schleicher D. R. G., Schmidt W., Niemeyer J., 2013c, ApJ, 772, L3
Latif M. A., Schleicher D. R. G., Schmidt W., Niemeyer J., 2013d, MNRAS, 432, 668
Latif M. A., Schleicher D. R. G., Schmidt W., Niemeyer J. C., 2013e, MNRAS, 436, 2989
Latif M. A., Schleicher D. R. G., Spaans M., Zaroubi S., 2011, A&A, 532, A66
Latif M. A., Zaroubi S., Spaans M., 2011, MNRAS, 411, 1659
Leitherer C., Schaerer D., Goldader J. D., Delgado R. M. G., Robert C., Kune D. F., de Mello D. F., Devost D., Heckman T. M., 1999, ApJS, 123, 3
Lodato G., Natarajan P., 2006, MNRAS, 371, 1813
Lupi A., Colpi M., Devecchi B., Galanti G., Volonteri M., 2014, MNRAS, 442, 3616
Madau P., Haardt F., Dotti M., 2014, ApJ, 784, L38
Martin P. G., Schwarz D. H., Mandy M. E., 1996a, ApJ, 461, 265
Martin P. G., Schwarz D. H., Mandy M. E., 1996b, ApJ, 461, 265
Meijerink R., Spaans M., 2005, A&A, 436, 397
Mitchell G. F., Deveau T. J., 1983, ApJ, 266, 646
Miyake S., Stancil P. C., Sadeghpour H. R., Dalgarno A., McLaughlin B. M., Forrey R. C., 2010, ApJL, 709, L168
Mortlock D. J., Warren S. J., Venemans B. P., Patel M., Hewett P. C., McMahon R. G., Simpson C., Theuns T., Gonzáles-Solares E. A., Adamson A., Dye S., Hambly N. C., Hirst P., Irwin M. J., Kuiper E., Lawrence A., Röttgering H. J. A., 2011, Nature, 474, 616
Omukai K., 2000, ApJ, 534, 809
Omukai K., 2001, ApJ, 546, 635
Omukai K., Schneider R., Haiman Z., 2008, ApJ, 686, 801
Omukai K., Tsuribe T., Schneider R., Ferrara A., 2005, ApJ, 626, 627
Osterbrock D. E., 1989, Astrophysics of gaseous nebulae and active galactic nuclei

Poulaert G., Brouillard F., Claeys W., McGowan J. W., Van Wassenhove G., 1978, Journal of Physics B Atomic Molecular Physics, 11, L671
Regan J. A., Haehnelt M. G., 2009, MNRAS, 393, 858
Regan J. A., Johansson P. H., Haehnelt M. G., 2014, MNRAS, 439, 1160
Regan J. A., Johansson P. H., Wise J. H., 2014, ArXiv e-prints:1407.4472
Ricotti M., Gnedin N. Y., Shull J. M., 2002, ApJ, 575, 33
Ricotti M., Ostriker J. P., 2004, MNRAS, 352, 547
Safranek-Shrader C., Milosavljević M., Bromm V., 2014, MNRAS, 440, L76
Salvaterra R., Haardt F., Volonteri M., 2007, MNRAS, 374, 761
Savin D. W., Krstić P. S., Haiman Z., Stancil P. C., 2004, ApJL, 606, L167
Schaerer D., 2003, A&A, 397, 527
Schleicher D. R. G., Palla F., Ferrara A., Galli D., Latif M., 2013, A&A, 558, A59
Schleicher D. R. G., Spaans M., Glover S. C. O., 2010, ApJ, 712, L69
Schober J., Schleicher D. R. G., Klessen R. S., 2014, ArXiv e-prints:1404.2578
Sethi S., Haiman Z., Pandey K., 2010, ApJ, 721, 615
Shang C., Bryan G. L., Haiman Z., 2010, MNRAS, 402, 1249
Shapiro P. R., Kang H., 1987, ApJ, 318, 32
Shull J. M., van Steenberg M. E., 1985, ApJ, 298, 268
Spaans M., Silk J., 2006, ApJ, 652, 902
Stenrup M., Larson Å., Elander N., 2009, ArXiv e-prints:0902.1900
Sugimura K., Omukai K., Inoue A. K., 2014, ArXiv e-prints
Susa H., Hasegawa K., Tominaga N., 2014, ApJ, 792, 32
Tanaka T., Haiman Z., 2009, ApJ, 696, 1798
Turk M. J., Smith B. D., Oishi J. S., Skory S., Skillman S. W., Abel T., Norman M. L., 2011, ApJS, 192, 9
Valdés M., Ferrara A., 2008, MNRAS, 387, L8
Van Borm C., Spaans M., 2013, A&A, 553, L9
Venemans B. P., Findlay J. R., Sutherland W. J., De Rosa G., McMahon R. G., Simcoe R., González-Solares E. A., Kuijken K., Lewis J. R., 2013, ApJ, 779, 24
Verner D. A., Ferland G. J., 1996, ApJS, 103, 467
Verner D. A., Ferland G. J., Korista K. T., Yakovlev D. G., 1996, ApJ, 465, 487
Visbal E., Haiman Z., Bryan G. L., 2014, ArXiv e-prints:1406.7020
Volonteri M., 2010, A&A Rev., 18, 279
Willott C. J., Delorme P., Reylé C., Albert L., Bergeron J., Crampton D., Delfosse X., Forveille T., Hutchings J. B., McLure R. J., Omont A., Schade D., 2010, AJ, 139, 906
Wise J. H., Turk M. J., Abel T., 2008, ApJ, 682, 745
Wishart A. W., 1979, MNRAS, 187, 59P
Wolcott-Green J., Haiman Z., Bryan G. L., 2011, MNRAS, 418, 838
Wolfire M. G., Hollenbach D., McKee C. F., Tielens A. G. G. M., Bakes E. L. O., 1995, ApJ, 443, 152
Wutschik S., Schleicher D. R. G., Palmer T. S., 2013, A&A, 560, A34
Yoshida N., Omukai K., Hernquist L., Abel T., 2006, ApJ, 652, 6

APPENDIX A:

A1 Chemical Model

The details of our chemical model are described in the following subsections. The chemical reactions and their rate coefficients are listed in table 1.

A2 Photochemistry

For the photo-dissociation of H_2, we use the rate provided by Glover & Jappsen (2007) and multiply it with the Lyman Werner flux centered at $h\overline{\nu}$=12.87 eV normalized by the spectrum at Lyman limit as the absorption of Lyman Werner photons occurs in the narrow frequency range 12.24eV < $h\,\nu$ < 13.51 eV (Abel et al. 1997; Glover & Jappsen 2007). It is further re-scaled by J_{21}

$$k_{\rm H_2}[T_{\rm rad}] = 1.38\times10^{-12} J_{21} \frac{B(12.87\ {\rm eV}, T_{\rm rad})}{B(13.6\ {\rm eV}, T_{\rm rad})} \qquad [s^{-1}] \quad \text{(A1)}$$

here $B(E, T_{\rm rad})$ is the black-body spectrum and is defined as:

$$B(E, T_{\rm rad}) = \frac{2E^3}{h^2c^2}\frac{1}{(e^{E/k_bT_{\rm rad}}-1)} \quad \text{(A2)}$$

where h is the Planck constant, c the speed of light, and k_b the Boltzmann constant. The rate is computed by assuming that H_2 molecule is in the roto-vibrational ground state ($\nu = 0, J = 0$). However, relaxing this assumption does not strongly affect the final rate (Glover & Jappsen 2007).

For the H^- photo-detachment cross-section, we use recent data which includes the absorption of the H^- resonance states near 11 eV (Stancil P. private communication, similar to Miyake et al. 2010). These contributions were neglected in previous calculation of the rate by Wishart 1979. We note that by taking into account this contribution does not change the final rate significantly. The H^- photo-detachment rate is evaluated by integrating the cross-section over different radiation black-body spectra normalized at 13.6 eV in the following way:

$$k_{\rm H^-}[T_{\rm rad}] = 6.2415\times10^{-10} J_{21} \frac{\frac{4\pi}{h}\int_{0.76}^{13.6}\frac{\sigma(E)}{E}B(E, T_{\rm rad})dE}{B(13.6\ {\rm eV}, T_{\rm rad})} \quad \text{(A3)}$$

The photo-dissociation of H_2^+ is computed in a similar way and the cross-section is reported in table 1.

A3 X-ray physics

The impact of X-ray heating and ionization on hydrogen and helium atoms has been investigated in many studies (Shull & van Steenberg 1985; Wolfire et al. 1995; Ricotti et al. 2002; Ricotti & Ostriker 2004; Meijerink & Spaans 2005; Valdés & Ferrara 2008; Furlanetto & Stoever 2010). The primary photo-ionization produces energetic electrons which can subsequently cause a secondary ionization of atoms. The total (primary + secondary) photo ionization rate is

$$\zeta^i_{tot} = \zeta^i_p + \sum_{j={\rm H,He}} \frac{n_j}{n_i}\zeta^j_p\langle\phi^i\rangle \quad \text{(A4)}$$

where the index p stands for the primary, n is the number density of the given specie, i represents H and He. The second term on the right hand side shows the contribution of

secondary ionization. The primary photo-ionization rate ζ_p^i is

$$\zeta_p^i = \frac{4\pi}{h} \int \frac{J_X(E)}{E} e^{-\tau(E)} \sigma^i(E) dE. \quad \text{(A5)}$$

The flux $J_X(E)$ is given in equation 5, σ^i are the photo-ionization cross sections of H and He and are taken from Verner & Ferland (1996). It is worth noting that the cross section for He given by Osterbrock (1989) and employed in Inayoshi & Omukai (2011b) is few orders of magnitude higher. This results in higher photo-heating/photo-ionization and reduces the value of $J_{X,21}$ to become effective for $J_{21}^{\rm crit}$ as already discussed in the results section.

Here τ is the opacity expressed as (Inayoshi & Omukai 2011b)

$$\tau(E) = \sum_{i=\rm H,He} \sigma^i(E) N_i \quad \text{(A6)}$$

N_i is the column density defined as

$$N_i = n_i \lambda_J \quad \text{(A7)}$$

where λ_j is the Jeans length defined as

$$\lambda_J = \sqrt{\frac{\pi k_b T}{G \rho \mu m_H}} \quad \text{(A8)}$$

G the gravitational constant, m_H the proton mass, ρ the total mass density, and μ the mean molecular weight evaluated as

$$\mu = \frac{\sum_k \rho_k}{\rho} \quad \text{(A9)}$$

here k represents all the species.

The number of secondary ionization of H and He per primary ionization, ϕ^H and ϕ^{He} are taken from Shull & van Steenberg (1985) and are defined as:

$$\phi^H(E, x_e) = \left(\frac{E}{13.6 \text{ eV}} - 1\right) 0.3908 (1 - x_e^{0.4092})^{1.7592} \quad \text{(A10)}$$

$$\phi^{He}(E, x_e) = \left(\frac{E}{24.6 \text{ eV}} - 1\right) 0.0554 (1 - x_e^{0.4614})^{1.666} \quad \text{(A11)}$$

where x_e is the electron fraction.

The above quantities are then averaged over the X-rays spectrum as

$$\langle \phi^i \rangle = \frac{\int J_X(E) \phi^i(E, x_e) dE}{\int J_X(E) dE} \quad \text{(A12)}$$

and are used in eq. A4. The fitting formulas for the secondary ionization given in equations A10 & A11 are valid for energy $E > 100$ eV and for a gas mixture of H and He.

The photo-ionization heating is given by

$$\Gamma = \Gamma^{\rm H} + \Gamma^{\rm He} \quad \text{(A13)}$$

where Γ^i is defined as following

$$\Gamma^i = \frac{4\pi}{h} \int \frac{J_X(E)}{E} e^{-\tau(E)} \sigma^i(E) E_h^i(E, x_e) dE \quad \text{(A14)}$$

with $E_h^i(E, x_e)$ is the fraction of primary electron energy which goes into heating (Shull & van Steenberg 1985). The heating is given in units of eV s^{-1}.

$$E_h^i(E, x_e) = (E - E_0^i) 0.9971 [1 - (1 - x_e^{0.2663})^{1.3163}] \quad \text{(A15)}$$

with i = H, He, $E_0^{\rm H} = 13.6$ eV, and $E_0^{\rm He} = 24.6$ eV.

Rates & reactions used in this study are listed in table below.

Table 1. The list of reactions and rates included in our chemical network. Here T is the gas temperature in K while T_e is the gas temperature in eV.

Reaction	Rate coefficient (cm^3 s^{-1})		Ref.
(1) H + e$^-$ → H$^+$ + 2e$^-$	k_1 = exp[-32.71396786+13.5365560 ln T_e - 5.73932875 (ln T_e)^2+1.56315498 (ln T_e)^3 - 0.28770560 (ln T_e)^4+3.48255977 × 10^{-2}(ln T_e)^5 - 2.63197617 × 10^{-3}(ln T_e)^6+1.11954395 × 10^{-4}(ln T_e)^7 - 2.03914985 × 10^{-6}(ln T_e)^8]		1
(2) H$^+$ + e$^-$ → H + γ	$k_2 = 3.92 \times 10^{-13}\ T_e^{\ -0.6353}$	$T \leq 5500$ K	2
	k_2 = exp[-28.61303380689232 - 7.241 125 657 826 851 × 10^{-1} ln T_e - 2.026 044 731 984 691 × 10^{-2} (ln T_e)^2 - 2.380 861 877 349 834 × 10^{-3} (ln T_e)^3 - 3.212 605 213 188 796 × 10^{-4} (ln T_e)^4 - 1.421 502 914 054 107 × 10^{-5} (ln T_e)^5 + 4.989 108 920 299 510 × 10^{-6} (ln T_e)^6 + 5.755 614 137 575 750 × 10^{-7} (ln T_e)^7 - 1.856 767 039 775 260 × 10^{-8} (ln T_e)^8 - 3.071 135 243 196 590 × 10^{-9} (ln T_e)^9]	$T > 5500$ K	
(3) He + e$^-$ → He$^+$ + 2e$^-$	k_3 = exp[-44.09864886 + 23.915 965 63 lnT_e - 10.753 230 2 (ln T_e)^2 + 3.058 038 75 (ln T_e)^3 - 5.685 118 9 × 10^{-1} (ln T_e)^4 + 6.795 391 23 × 10^{-2} (ln T_e)^5 - 5.009 056 10 × 10^{-3} (ln T_e)^6 + 2.067 236 16 × 10^{-4} (lnT_e)^7 - 3.649 161 41 × 10^{-6} (ln T_e)^8]	$T_e > 0.8$ eV	1
(4) He$^+$ + e$^-$ → He + γ	$k_4 = 3.92 \times 10^{-13}\ T_e^{\ -0.6353}$	$T_e \leq 0.8$ eV	3
	k_4 = + 3.92 × 10^{-13} $T_e^{-0.6353}$ + 1.54 × 10^{-9} $T_e^{-1.5}$ [1.0 + 0.3 / exp(8.099 328 789 667/T_e)] /[exp(40.496 643 948 336 62/T_e)]	$T > 0.8$ eV	
(5) He$^+$ + e$^-$ → He^{++} + 2e$^-$	k_5 = exp[-68.710 409 902 120 01 + 43.933 476 326 35 lnT_e - 18.480 669 935 68 (ln T_e)^2 + 4.701 626 486 759 002 (ln T_e)^3 - 7.692 466 334 492 × 10^{-1} (ln T_e)^4 + 8.113 042 097 303 × 10^{-2} (ln T_e)^5 - 5.324 020 628 287 001 × 10^{-3} (ln T_e)^6 + 1.975 705 312 221 × 10^{-4} (ln T_e)^7 - 3.165581065665 × 10^{-6} (ln T_e)^8]	$T_e > 0.8$ eV	4
(6) He^{++} + e$^-$ → He$^+$ + γ	$k_6 = 1.891 \times 10^{-10}/[1 + \sqrt{T/9.37}]^{0.2476}/[1 + \sqrt{T/(2.774 \times 10^6)}]^{1.7524}/\sqrt{T/9.37}$		5
(7) H + e → H$^-$ + γ	$k_7 = 1.4 \times 10^{-18} T^{0.928} \exp(-T/16200)$		6
(8) H$^-$ + H → H$_2$ + e$^-$	$k_8 = a_1(T^{a_2} + a_3 T^{a_4} + a_5 T^{a_6})/(1 + a_7 T^{a_8} + a_9 T^{a_{10}} + a_{11} T^{a_{12}})$ $a_1 = 10^{-10}$ $a_2 = 9.8493 \times 10^{-2}$ $a_3 = 3.2852 \times 10^{-1}$ $a_4 = 5.5610 \times 10^{-1}$ $a_5 = 2.7710 \times 10^{-7}$ $a_6 = 2.1826$ $a_7 = 6.1910 \times 10^{-3}$ $a_8 = 1.0461$ $a_9 = 8.9712 \times 10^{-11}$ $a_{10} = 3.0424$ $a_{11} = 3.2576 \times 10^{-14}$ $a_{12} = 3.7741$		7
(9) H + H$^+$ → H$_2^+$ + γ	$k_9 = 2.10 \times 10^{-20}(T/30)^{-0.15}$	$T < 30$ K	8
	dex[$-18.20 - 3.194 \log_{10} T + 1.786(\log_{10} T)^2 - 0.2072(\log_{10} T)^3$]	$T \geq 30$ K	

1: Janev et al. (1987), 2: Abel et al. (1997) fit by data from Ferland et al. (1992), 3: Cen (1992); Aldrovandi & Pequignot (1973)
4: Aladdin database, see Abel et al. (1997), 5: Verner & Ferland (1996), 6: de Jong (1972), 7: Kreckel et al. (2010)
8: Coppola et al. (2011)

Table 1 – *continued* The list of reactions and rates included in our chemical network. Here T is the gas temperature in K while T_e is the gas temperature in eV.

Reaction	Rate coefficient (cm^3 s^{-1})		Ref.
(10) $H_2^+ + H \rightarrow H_2 + H^+$	$k_{10} = 6.0 \times 10^{-10}$		9
(11) $H_2 + H^+ \rightarrow H_2^+ + H$	$k_{11} = [b_1 + b_2 \ln(T) + b_3(\ln(T))^2 + b_4(\ln(T))^3 + b_5(\ln(T))^4 + b_6(\ln(T))^5$		10
	$+b_7(\ln(T))^6 + b_8(\ln(T))^7] \exp(-a/T)$		
	$a = 2.1237150 \times 10^4$		
	$b_1 = -3.3232183 \times 10^{-7}$		
	$b_2 = 3.3735382 \times 10^{-7}$		
	$b_3 = -1.4491368 \times 10^{-7}$		
	$b_4 = 3.4172805 \times 10^{-8}$		
	$b_5 = -4.7813728 \times 10^{-9}$		
	$b_6 = 3.9731542 \times 10^{-10}$		
	$b_7 = -1.8171411 \times 10^{-11}$		
	$b_8 = 3.5311932 \times 10^{-13}$		
(12) $H^- + e^- \rightarrow H + 2e^-$	$k_{12} = \exp$[-18.018 493 342 73		1
	+ 2.360 852 208 681 lnT_e		
	- 2.827 443 061 704 $\times 10^{-1}$ (ln T_e)^2		
	+ 1.623 316 639 567 $\times 10^{-2}$ (ln T_e)^3		
	- 3.365 012 031 362 999 $\times 10^{-2}$ (ln T_e)^4		
	+ 1.178 329 782 711 $\times 10^{-2}$ (ln T_e)^5		
	- 1.656 194 699 504 $\times 10^{-3}$ (ln T_e)^6		
	+ 1.068 275 202 678 $\times 10^{-4}$ (ln T_e)^7		
	- 2.631 285 809 207 $\times 10^{-6}$ (ln T_e)^8]		
(13) $H^- + H \rightarrow 2H + e^-$	$k_{13} = 2.56 \times 10^{-9}\ T_e^{1.78186}$	$T_e \leq 0.04$ eV	11
	$k_{13} = \exp$[-20.372 608 965 333 24	$T_e > 0.04$ eV	
	+ 1.139 449 335 841 631 ln T_e		
	- 1.421 013 521 554 148 $\times 10^{-1}$ (ln T_e)^2		
	+ 8.464 455 386 63 $\times 10^{-3}$ (ln T_e)^3		
	- 1.432 764 121 299 2 $\times 10^{-3}$ (ln T_e)^4		
	+2.012 250 284 791 $\times 10^{-4}$ (ln T_e)^5		
	+ 8.663 963 243 09 $\times 10^{-5}$ (ln T_e)^6		
	- 2.585 009 680 264 $\times 10^{-5}$ (ln T_e)^7		
	+ 2.455 501 197 039 2 $\times 10^{-6}$ (ln T_e)^8		
	- 8.068 382 461 18 $\times 10^{-8}$ (ln T_e)^9]		
(14) $H^- + H^+ \rightarrow 2H + \gamma$	$k_{14} = 2.96 \times 10^{-6}/\sqrt{T} - 1.73 \times 10^{-9} + 2.50 \times 10^{-10}\sqrt{T} - 7.77 \times 10^{-13} T$		12
(15) $H^- + H^+ \rightarrow H_2^+ + e^-$	$k_{15} = 10^{-8} \times T^{-0.4}$		13
(16) $H_2^+ + e \rightarrow 2H + \gamma$	$k_{16} = 10^6(4.2278 \times 10^{-14} - 2.3088 \times 10^{-17} T + 7.3428 \times 10^{-21} T^2 - 7.5474 \times 10^{-25} T^3$		8
	$+3.3468 \times 10^{-29} T^4 - 5.528 \times 10^{-34} T^5)$		
(17) $H_2^+ + H^- \rightarrow H + H_2$	$k_{17} = 5.0 \times 10^{-7}\ \sqrt{10^2/T}$		14
(18) $3H \rightarrow H_2 + H$	$k_{18} = 6 \times 10^{-32} T^{-0.25} + 2 \times 10^{-31} T^{-0.5}$		15
(19) $H_2 + H \rightarrow 3H$	k_{19}, see ref.		16
(20) $H_2 + H + H \rightarrow H_2 + H_2$	$k_{20} = k_{18}/8$		17
(21) $H_2 + H_2 \rightarrow H_2 + H + H$	$k_{21} = kh_{21}^{(1-a_{21})} kl_{21}^{a_{21}}$		18
	$kl_{21} = 1.18 \times 10^{-10} \exp(-6.95 \times 10^4/T)$		
	$kh_{21} = 8.125 \times 10^{-8} T^{-0.5} \exp(-5.2 \times 10^4/T)(1 - \exp(-6 \times 10^3/T))$		
	$ncr_{21} = \mathrm{dex}[4.845 - 1.3 \log_{10}(T/10^4) + 1.62[\log_{10}(T/10^4)]^2]$		
	$a_{21} = 1/(1 + (\mathrm{nH}/ncr_{21}))$		
(22) $He^+ + H \rightarrow He + H^+$	$k_{22} = 1.20 \times 10^{-15}(T/300)^{0.25}$		19
(23) $He + H^+ \rightarrow He^+ + H$	$k_{23} = 1.26 \times 10^{-9} T^{-0.75} \exp(-1.275 \times 10^5/T)$	$T \leq 10^4$ K	19
	$k_{24} = 4 \times 10^{-37} T^{4.74}$	$T > 10^4$ K	
(24) $H_2 + e^- \rightarrow H + H + e^-$	$k_{24} = 4.38 \times 10^{-10} T^{0.35} \exp(-102000/T)$		20
(25) $H_2 + e^- \rightarrow H + H^-$	$k_{25} = 35.5 \times T^{-2.28} \exp(-46707/T)$		21
(26) $H_2 + \gamma \rightarrow H + H$	$k_{26} = 1.38 \times 10^9$	in units of s^{-1}	22
(27) $H_2^+ + \gamma \rightarrow H + H^+$	$\sigma = \mathrm{dex}[-40.97 + 6.03E - 0.504E^2 + 1.387 \times 10^{-2} E^3]$	2.65 eV $< E <$ 11.27 eV	23
	$\sigma = \mathrm{dex}[-30.26 + 2.79E - 0.184E^2 + 3.535 \times 10^{-3} E^3]$	11.27 eV $< E <$ 21.0 eV	
(28) $H^- + \gamma \rightarrow H + e^-$	private communication P. Stancil, 2014	see text	24
(29) $H + \gamma \rightarrow H^+ + e^-$	fit parameters from 5		5
(30) $He + \gamma \rightarrow He^+ + e^-$	fit parameters from 5		5

9 Karpas et al. (1979), 10: Savin et al. (2004), 11: Abel et al. (1997) based on Janev et al. (1987), 12: Stenrup et al. (2009), 13: Poulaert et al. (1978), 14: Dalgarno & Lepp (1987), 15: Forrey (2013), 16: Martin et al. (1996b), 17: rescaled following Glover & Abel (2008b)

18: Omukai (2000), 19: Yoshida et al. (2006), 20: Mitchell & Deveau (1983) fit of data by Corrigan (1965), 21: Capitelli et al. (2007), 22: Glover & Jappsen (2007), 23: Shapiro & Kang (1987), originally from Dunn (1968), 24: see also Miyake et al. (2010)